RESEARCH ARTICLE

Biochemical characterization of *Mycobacterium tuberculosis* dihydroorotate dehydrogenase and identification of a selective inhibitor

Marta Alberti[1], Stefano Sainas[2], Erika Ronchi[1], Marco L. Lolli[2], Donatella Boschi[2], Menico Rizzi[1], Davide M. Ferraris[1] and Riccardo Miggiano[1] (iD)

1 Department of Pharmaceutical Sciences, University of Eastern Piedmont, Novara, Italy
2 Department of Sciences and Drug Technology, University of Turin, Torino, Italy

Correspondence
R. Miggiano, Department of Pharmaceutical Sciences, University of Eastern Piedmont, Via Bovio 6, 28100 Novara, Italy
Tel: +390 321 375 813
E-mail: riccardo.miggiano@uniupo.it

Mycobacterium tuberculosis (MTB) is the etiologic agent of tuberculosis (TB), an ancient disease which causes 1.5 million deaths worldwide. Dihydroorotate dehydrogenase (DHODH) is a key enzyme of the MTB *de novo* pyrimidine biosynthesis pathway, and it is essential for MTB growth *in vitro*, hence representing a promising drug target. We present: (i) the biochemical characterization of the full-length MTB DHODH, including the analysis of the kinetic parameters, and (ii) the previously unreleased crystal structure of the protein that allowed us to rationally screen our in-house chemical library and identify the first selective inhibitor of mycobacterial DHODH. The inhibitor has fluorescence properties, potentially instrumental to *in cellulo* imaging studies, and exhibits an IC$_{50}$ value of 43 μM, paving the way to hit-to-lead process.

Keywords: dihydroorotate dehydrogenase; drug discovery; *Mycobacterium tuberculosis*; pyrimidine biosynthesis; *tuberculosis*

Tuberculosis (TB) is an infectious disease caused by *Mycobacterium tuberculosis* (MTB) that nowadays still claims more than 1.5 million deaths worldwide, making MTB the world's top infectious killer. According to the most recent Global Tuberculosis Report (2022), the COVID-19 pandemic made the TB management even more difficult, reversing years of progress against the disease by increasing the number of TB deaths for the first time after a decade [1]. Moreover, the global scenario is becoming more alarming if we consider the spreading of multidrug-resistant (MDR) MTB strains, mostly referred to as rifampicin/isoniazid-resistant TB, as well as extensively drug-resistant (XDR) MTB strains that are resistant to first- and second-line antitubercular drugs [2]. In this context, where also the

adherence to the available long-term antitubercular treatments is poor, the development of antitubercular agents is in high demand as well as the identification of innovative molecular targets guided by the genotypic information derived from MTB genome sequencing [3].

Pyrimidine biosynthesis pathway represents a valid source of therapeutic targets since dysfunctions in nucleotide metabolism are detrimental for bacterial survival because vital for proliferation and for bacterial growth in human blood during septicemia [4–8]. While nondividing cells satisfy their need in pyrimidines through a salvage pathway (Fig. 1A), proliferating cells and infecting pathogens fulfill their large demand for nucleotide precursors with the *de novo* pathway (Fig. 1A) [5],

Abbreviations
DHO, dihydroorotate; DHODH, dihydroorotate dehydrogenase; FMN, flavin mononucleotide; HDT, host-directed therapies; DCIP, 2, 6-dichloroindophenol; MDR, multidrug resistant; MQ, menaquinone; MTB, *Mycobacterium tuberculosis*; ORO, orotate; PDT, pathogen-directed therapies; TB, tuberculosis; XDR, extensively drug resistant.
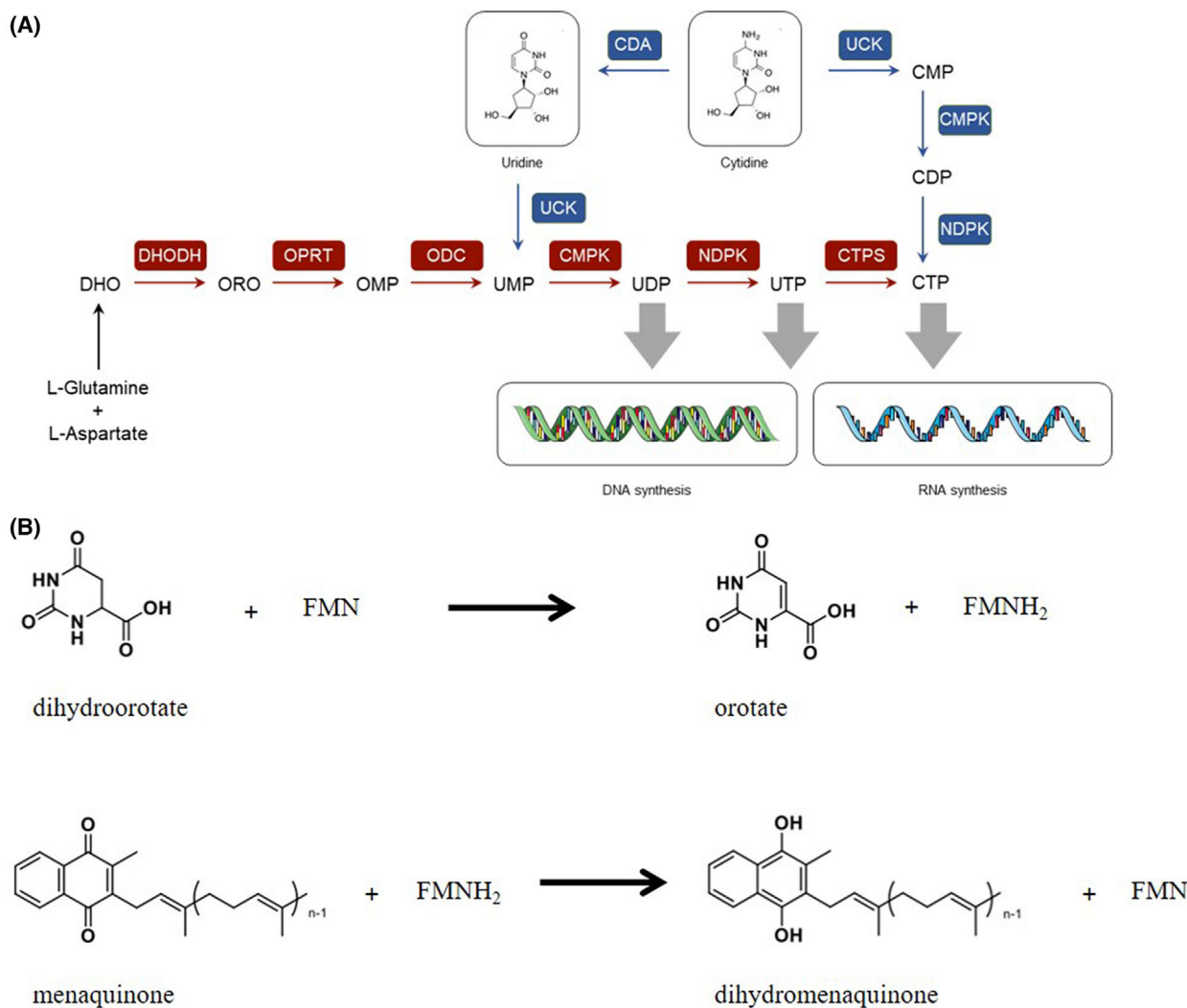
Fig. 1. (A) Schematic representation of *de novo* (red) and salvage (blue) pyrimidine biosynthesis pathway. CDA, cytidine deaminase; CDP, cytidine diphosphate; CMP, cytidine monophosphate; CMPK, cytidine monophosphate kinase; CTP, cytidine triphosphate; CTPS, CTP synthetase; DHO, dihydroorotate; DHODH, dihydroorotate dehydrogenase; NDPK, nucleoside-diphosphate kinase; ODC, orotidine-5′-phosphate decarboxylase; OMP, orotidine 5′-monophosphate; OPRT, orotate phosphoribosyltransferase; ORO, orotate; UCK, uridine/cytidine kinase; UDP, uridine diphosphate; UMP, uridine monophosphate; UTP, uridine triphosphate. (B) Scheme of *Mt*DHODH reaction with chemical formulae. Electron transfer from dihydroorotate to FMN and subsequent transfer onto menaquinone (MQ).

consisting in a multienzymatic cascade that culminates in the production of uridine monophosphate (UMP), the precursor of all pyrimidine nucleotides [9]. In MTB, the genes encoding five of the enzymes involved in the pyrimidine biosynthesis belong to the *pyr* operon and are essential for the growth of MTB *in vitro* [9,10]. However, most of the knowledge of the biochemistry of pyrimidine biosynthesis in MTB comes from studies performed on reference bacteria.

The fourth step in the *de novo* pathway refers to the oxidation of dihydroorotate (DHO) to orotate (ORO), and it is carried out by the rate-limiting flavoenzyme dihydroorotate dehydrogenase (DHODH), encoded by

the gene *pyrD* (Rv2139) that catalyzes the formation of the 5,6-insaturation of the pyrimidine base. The reaction proceeds through a ping-pong mechanism where the flavin mononucleotide (FMN) is firstly reduced into $FMNH_2$, and then it is oxidized again to FMN by a third molecule that acts as an electron acceptor.

DHODHs are divided into class 1 and class 2, depending on sequence similarity, subcellular location and substrate preference [11]. DHODHs belonging to class 1 are cytosolic enzymes and are divided into class 1A and class 1B, which differ for the structural and mechanistic features because they use fumarate [12,13] and NAD^+

[14] as electron acceptors, respectively. On the contrary, class 2 enzymes are monomeric proteins that exploit the N-terminal hydrophobic region to be anchored to the inner membrane of the mitochondria in eukaryotes [15,16], and in the cytosolic membrane in some prokaryotes [17]. For class 2 proteins, the FMN cofactor is regenerated by transferring electrons to ubiquinone in humans or to menaquinone (MQ) in MTB. Indeed, MQs (2-methyl-3-polyprenyl-1, 4-naphthoquinones) are the predominant lipoquinones of mycobacteria since they lack the pathway for the synthesis of ubiquinone [11,18]. Since MTB is an intracellular pathogen, it could potentially respond to MQ auxotrophy by salvaging the ubiquinone from the human host; consequently, demonstrating the MTB DHODH (*Mt*DHODH) selectivity toward different lipoquinones will add insights to the complexity of MTB life cycle and crosstalk with the host. Prokaryotic DHODHs are considered potential drug targets in conventional pathogen-directed therapies (PDT). The ubiquinone-binding site in human DHODH (*h*DHODH) is known to be significantly divergent from its parasitic counterpart and, several groups have reported the discovery of pathogen-specific DHODH inhibitors (*Helicobacter pylori*, *Toxoplasma gondii*, *Plasmodium falciparum*, and *Schistosoma mansoni*) [19]. Notably, phase Ia/Ib clinical studies of the potent and specific *Plasmodium falciparum* DHODH inhibitor DSM265 have recently been published with promising results [20].

Moreover, combining host-directed therapy (HDT) and PDT strategies represents a potentially effective method for lowering the insurgence of drug-resistant strains and for shortening the duration of the therapies, a common problem of conventional TB treatments.

MTB *pyrD* is essential for MTB growth *in vitro* [21], hence representing a promising drug target in a PDT, that can be potentially combined with HDT targeting human *h*DHODH. Indeed, unlike parasites such as *Helicobacter pylori*, *Plasmodium falciparum*, and *Schistosoma mansoni*, which lack salvage pathways for pyrimidine nucleotides, in MTB the pyrimidines are synthesized both through the *de novo* biosynthesis and via the salvage pathways under physiological conditions similarly to mammalian cells [22].

To the best of our knowledge, *Mt*DHODH is fully uncharacterized since the literature lacks data on the biochemical and structural characterization of the enzyme. In particular, the only structural model, which has been deposited in the protein data bank (PDB), refers to a truncated version of the protein (PDB: 4XQ6) not reported in a peer-reviewed, indexed scientific journal. The aim of the present work is to fill the gap between the potential druggability of the enzyme

and the lack of biochemical data. Accordingly, herein we present the crystallographic structure of *Mt*DHODH coupled with the biochemical investigation of the protein. Moreover, a structure-based inhibitor screening allowed us to identify the first *Mt*DHODH inhibitor that showed also fluorescent properties, potentially instrumental to *in cellulo* imaging studies, paving the way to the development of a new class of antimycobacterial agents with fluorescent properties, with interesting applicative perspectives.

Materials and methods

Chemicals

All reagents were obtained from commercial suppliers (Sigma Aldrich, St. Luois, MO, USA; Abcam, Cambridge, UK; Alfa Aesar, Haverhill, MA, USA; Fluorochem, Hadfield, UK) and used without further purification.

Proteins expression, purification, and crystallization

The open reading frame of *Mt*DHODH (identifier: RV2139) was subcloned into pET-28a(+) (GenScript, Piscataway, NJ, USA) plasmid using NdeI/XhoI recognized sequences as restriction sites. The plasmidic vector was designed to induce the expression of the recombinant N-terminal His-tagged protein (predicted molecular mass of 40 161 Da) exploiting *E. coli* BL21(DE3) (Novagen) as host system. *E. coli* was transformed with the target construct and grown on an agar plate for 16 h at 37 °C, and then cells were inoculated in 1 L of sterile 2XYT liquid broth in the presence of Kanamycin (50 μg/mL) as selector. Bacterial culture was grown in a 5 L shaking flask at 5 *g*/37 °C until they reached optical density at 600 nm (OD600) of 0.6. The expression of the recombinant *Mt*DHODH was induced with 0.2 mM isopropyl-1-thio-D-galactopyranoside, and cell suspension was further incubated at 5 *g*/16 °C for 15 h. Culture was harvested and centrifuged at 8 000 *g*/4 °C for 10 min 8 g of bacterial pellet were resuspended (1 g: 9 mL) in lysis buffer (LB) [100 mM HEPES pH 7,8, 300 mM NaCl, 10% (v/v) Glycerol, 0.1% (v/v) Triton X-100 and 1 mM ORO] supplemented with complete EDTA-free protease inhibitor cocktail (Merck) and DNAse. All the following steps were performed at 4 °C. Cells were lysed with a Sonics Vibra-Cell VC 130 Ultrasonic Homogenizer (Strokes: 8; Pulse: 30″; Stop: 1′; Amplitude: 45). The lysate was centrifuged at 64 000 *g*/4 °C for 50 min (Beckman Coulter Avanti Centrifuge J-26 XP), and the cleared cell lysate was loaded onto a Qiagen Ni-NTA Agarose column pre-equilibrated with LB supplemented with 10 mM imidazole. After washing the resin with 20 CV of the wash buffer (LB supplemented with 50 mM imidazole), the protein was eluted with the elution buffer (LB supplemented

with 300 mM imidazole). The fractions containing *Mt*DHODH resulted to be yellow since the presence of FMN prosthetic group directly bound to the protein core. The positive fractions, checked through 12.5% acrylamide SDS/PAGE, were pooled and concentrated using Amicon 15–10 000 MWCO centrifugal concentrator (Merck). Before undergoing crystallization studies, the concentrated protein was loaded onto a Hiload Superdex 200 16/600 (GE Healthcare, Chicago, IL, USA) column, pre-equilibrated with a size exclusion buffer [100 mM HEPES pH 7,8, 300 mM NaCl, 10% (v/v) Glycerol, % (v/v) Triton X-100 and 1 mM ORO]. Size exclusion chromatography was monitored at 350 and 442 nm wavelengths to avoid interference with the absorbance peak of ORO. Protein quantification was performed by Bradford assay in a calibrated system at 595 nm with a Savatec Onda spectrophotometer UV-21. Analytical size exclusion chromatography was performed using a Superdex 200 10/300 GL column (Cytiva), precalibrated with standard proteins (following manufacturer's instructions), and by fluxing the size exclusion buffer [100 mM HEPES pH 7,8, 300 mM NaCl, 10% (v/v) Glycerol 1 mM ORO and 0.25% n-Undecyl-N,N-Dimethylamine-N-Oxide (UDAO) w/v] as the mobile phase. To evaluate the stability of the protein, different aliquots of the *Mt*DHODH preparation [stock buffer: 100 mM HEPES pH 7,8, 300 mM NaCl, 10% (v/v) Glycerol, % (v/v) Triton X-100 and 1 mM ORO] have been stored for up to 1 week at different temperatures, before being analyzed by standard SDS/PAGE and differential scanning fluorimetry in order to compare the different stocks in terms of thermal denaturation in the presence of SYPRO Orange dye.

For crystallization assay, the purified protein was mixed with ORO to give a final concentration of 2 mM and incubated at 4 °C over night. 0.5 μL of the complex protein-ORO were mixed with 0.5 μL of reservoir solution from Classics II Suite (QIAGEN, Hilden, Germany) and underwent crystallization trials by means of robot-assisted (Oryx4; Douglas Instruments, Hangerford, UK), sitting-drop-based spare-matrix strategy. After 3 months, a single bar-shaped and fragile crystal grew in G1 drop condition (0.2 M Sodium Chloride, 0.1 M Tris–HCl pH 8.5 and 25% (w/v) PEG 3350).

X-ray data collection, structure determination, and refinement

The crystal was cryoprotected with 12.5% (v/v) Glycerol, flash-cooled in liquid nitrogen and sent to the European Synchrotron Radiation Facility (ESRF), France, where they underwent X-ray diffraction experiment on the beamline ID23-2 with a Pixel Pilatus3_2M as detector [23].

The data were indexed using XDS program; then they were integrated and scaled to a resolution of 3.8 Å using the Aimless utilities of the CCP4i2 Program Suite version 8.0.008 [24]. The crystal was assigned to the orthorhombic space group $P2_12_12_1$ with the cell dimensions a = 46.0 Å,

Table 1. Data collection and refinement statistics.

Resolution range	41.5–3.8 (3.9–3.8)
Space group	P 21 21 21
Unit cell	46.0 85.2180.9 90 90 90
Total reflections	13 712 (1318)
Unique reflections	7193 (699)
Multiplicity	1.9 (1.9)
Completeness (%)	95.85 (96.53)
Mean I/sigma(I)	5.02 (1.31)
Wilson B-factor	116.10
R-merge	0.116 (0.59)
R-meas	0.15 (0.83)
R-pim	0.11(0.5892)
CC1/2	0.99 (0.77)
CC*	0.99 (0.93)
Reflections used in refinement	7190 (696)
Reflections used for R-free	371 (44)
R-work	0.29 (0.40)
R-free	0.33 (0.35)
CC(work)	0.89 (0.69)
CC(free)	0.93 (0.79)
Number of nonhydrogen atoms	5254
Macromolecules	5192
Ligands	62
Solvent	0
Protein residues	692
RMS(bonds)	0.003
RMS(angles)	0.73
Ramachandran favored (%)	98.24
Ramachandran allowed (%)	1.76
Ramachandran outliers (%)	0.00
Rotamer outliers (%)	0.00
Clashscore	15.84
Average B-factor	126.15
Macromolecules	126.57
Ligands	91.40
Number of TLS groups	1

Statistics for the highest-resolution shell are shown in parentheses.

b = 85.2 Å, c = 180.9 Å, containing 2 molecules in the asymmetric unit, with a Matthews coefficient and a solvent percentage of 2.21 Å^3 Da^{-1} and 44.40%, respectively (Table 1).

The structure was determined by molecular replacement with phenix-PHASER [25] using the predicted structure provided from Alphafold database as a search model (AF-P9WHL1-F1-model). Manual model building was performed with Coot program [26], structure refinement was done with PHENIX [25], and pictures were generated with PyMol [27]. Data collection and refinement statistics are listed in Table 1.

PDB deposition

The atomic coordinates and structure factors of *Mt*DHODH have been deposited in the Protein Data Bank (PDB) as 8OFW code.

DHODH enzymatic and inhibition assays

The enzymatic activity of both *Mt*DHODH and *h*DHODH was monitored using a Tecan Sunrise spectrophotometer in a coupled reaction which involves the reduction of 2, 6-dichloroindophenol (DCIP) reagent. The reduction of DCIP is stoichiometrically associated with the enzymatic oxidation of one equivalent of the substrate DHO. The purified recombinant protein was tested at 0.1 μM alone or complex with the inhibitor MEDS322 (tested at increasing concentration from 12.5 to 300 μM). After 20 min of preincubation at 37 °C in the mixture of activity [50 mM Tris–HCl pH 8.0, 300 mM NaCl, 5% (v/v) Glycerol, 0,1% (v/v) Triton X-100, 50 μM DCIP, and 100 μM MQ (dissolved in DMSO)] up to a final volume of 100 μL, the reaction was initiated by addition of DHO at increasing concentration from 1.56 to 200 μM and the reduction was monitored at 600 nm for 10 min. For the calculation of the biochemical parameters toward MQ cofactor, the experimental setting was the same described above keeping the concentration of DHO fixed to 100 μM and varying the concentration of MQ from 12 to 400 μM. The curves were analyzed in their maximum drop in the first 5 min of the enzymatic reaction. Biochemical parameters were calculated using GraphPad Prism software.

Synthesis of MEDS322

Analytical grade solvents (diethyl ether, methanol [MeOH], glacial acetic acid) were used without further purification. When needed, solvents were dried on 4 Å molecular sieves. Thin layer chromatography (TLC) on silica gel was carried out on 5 × 20 cm plates with 0.25 mm layer thickness to monitor the process of reactions. Anhydrous Na_2SO_4 was used as a drying agent for the organic phases. Purification of compounds was achieved with flash column chromatography on silica gel (Kieselgel 60, 230–400 mesh ASTM; Merck) using the eluents indicated. Final compounds were assayed in biological experiments. Their purity was measured by HPLC analyses, showing a chromatogram where the main peak (area at least 95% of all detected peaks) was attributable to the final compound. Some HPLC analyses were performed on a UHPLC chromatographic system (Flexar; Perkin Elmer, Waltham, MA, USA). The analytical column was an UHPLC Acquity CSH Fluoro-Phenyl (2.1–100 mm, 1.7 mm particle size; Waters, Milford, MA, USA). Compounds were dissolved in acetonitrile or methanol and injected through a 20 mL loop. The mobile phase consisted of methanol/water with 0.1% trifluoroacetic acid; two gradient profiles of mobile phase were used to assay the purity of each compound. UHPLC analysis was run at flow rates of 0.5 mL/min, and the column effluent was monitored at 215 and 254 nm, referenced against a 360 nm wavelength. All compounds were routinely checked by ^{1}H- and ^{13}C-NMR and mass spectrometry. ^{1}H- and ^{13}C-NMR

spectra were performed on a Brüker 300 MHz Ultra shield spectrometer. For coupling patterns, the following abbreviations are used: br = broad, s = singlet, d = doublet, dd = doublet of doublets, t = triplet, q = quartet, and m = multiplet. MS spectra were performed on Finnigan-Mat TSQ-700 (70 eV, direct inlet for chemical ionization [CI]).

4-((3-Chlorophenyl)amino)thiazol-2(5H)-one [3]. 3-Chloroaniline (478 mg, 3.75 mmol) was added to a solution of isorhodanine 2 (500 mg, 3.75 mmol) in dry MeOH (5 mL), and then the reaction mixture was refluxed for 24 h. The reaction mixture was cooled at room temperature and the product was collected by filtration and washed with MeOH to yield the title compound as brown solid. Yield 47%. ^{1}H-NMR (300 MHz, DMSO-d_6): δ 4.54 (*s*, 2H); 7.11–7.63 (*m*, 3H, *aromatic protons*), 7.98 (*s*, 1H, *aromatic proton*), 11.13 (*s*, 1H, -NH). ^{13}C NMR (75 MHz, DMSO-d_6): δ 39.4, 118.7, 119.8, 124.4, 130.7, 133.3, 139.8, 176.7, 185.3. MS [CI, m/z]: 227 [M + H]$^+$.

Methyl-(Z)-2-(4-((4-((3-chlorophenyl)amino)-2-oxothiazol-5(2H)-ylidene)methyl)-2-methoxyphenoxy)acetate [4]. A solution of **3** (3.5 g, 15.44 mmol) in glacial acetic acid (15 mL) was added to a mixture of methyl 2-(4-formyl-2-methoxyphenoxy)acetate (1.73 g, 7.72 mmol) in glacial acetic acid (35 mL). The reaction mixture was heated to 100 °C for 3 h. Then, the reaction mixture was cooled at room temperature and a precipitation occurred. The solid was collected by filtration, washed with acetic acid, and then water. The crude compound was recrystallized with acetic acid and then washed with diethyl ether to afford the title compound as yellow solid. Yield 82%. ^{1}H-NMR (300 MHz, *DMSO-d_6*): δ 3.71 (*s*, 3H), 3.86 (*s*, 3H), 4.89 (*s*, 2H), 7.07 (*d*, J = 8.5 Hz, 1H), 7.13–7.22 (*m*, 2H), 7.28 (*d*, J = 7.8 Hz, 1H), 7.46 (*t*, J = 8.1 Hz, 1H), 7.76 (*d*, J = 8.0 Hz, 1H), 8.00 (*s*, 1H), 8.08 (*s*, 1H), 10.72 (*s*, 1H, -NH). ^{13}C NMR (75 MHz, *DMSO-d_6*): δ 51.8, 55.6, 65.0, 113.1, 113.6, 120.5, 121.7, 123.6, 125.0, 126.6, 127.5, 129.7, 130.4, 133.0, 139.6, 148.9, 149.0, 168.8, 170.4, 178.3. MS [CI, m/z]: 433 [M + H]$^+$.

(Z)-2-(4-((4-((3-Chlorophenyl)amino)-2-oxothiazol-5(2H)-ylidene)methyl)-2-methoxyphenoxy)acetic acid [1]. Aqueous 2 M NaOH (2 mL) was added to a suspension of compound **4** (500 mg, 1.15 mmol) in methanol (10 mL). The suspension was stirred for 30 min at room temperature, and then the obtained solution was diluted with water (20 mL) and acidified with 0.5 M HCl until to reach pH 2. The precipitate was filtered, washed with water, and crystallized with methanol. Yield 89%, yellow solid. ^{1}H-NMR (300 MHz, *DMSO-d_6*): δ 3.86 (*s*, 3H), 4.79 (*s*, 2H), 7.04 (*d*, J = 8.3 Hz, 1H), 7.14–7.22 (*m*, 2H), 7.29 (*d*, J = 7.9 Hz, 1H), 7.47 (*t*, J = 8.1 Hz, 1H), 7.76 (*d*, J = 8.0 Hz, 1H), 8.00 (*s*, 1H), 8.09 (*s*, 1H), 10.74 (*br s*, 1H, -NH), 13.14 (*br s*, 1H, -COO*H*). ^{13}C NMR (75 MHz, *DMSO-d_6*): δ 55.6, 64.8, 113.0, 113.2, 120.6, 121.7, 123.7, 125.1, 126.4, 127.1, 129.9, 130.5, 133.1, 139.7, 149.0, 149.2, 169.8, 170.4, 178.5. MS [CI, m/z]: 419 [M + H]$^+$.

RESULTS and DISCUSSION

Expression and purification of wild-type full-length *Mt*DHODH

As of today, 143 structures of DHODHs in 15 different organisms are described in Protein Data Bank (PDB); among which, however, MTB is missing. Indeed, *Mt*DHODH lacks a complete structural characterization because the only provided experimental model (PDB code: 4XQ6) is a N-terminal truncated version of the protein (Val31-Arg353) where the DNA coding for Met1-Ala30 residues was not included in the cloning vector.

In initial attempts, SDS/PAGE and western blot assays of the isolated enzyme revealed proteolytic degradation at the level of the N-terminal domain (data not shown). To overcome the issue, the addition of 1 mM ORO [28] and of twofold more of the protease inhibitor cocktail in the lysis buffer was enough to preserve the protein integrity. Moreover, the strongly hydrophobic nature of the outer additional residues made the full-length structure sticky and more prone to aggregation and, consequently, more susceptible to amorphous precipitation. In this regard, to avoid non-functional multimeric adducts, different ligands have been tested (i.e., 100 μM MQ, 0.25% w/v n-Undecyl-N,N-Dimethylamine-Oxide and 0.1% of triton X-100 as detergent). The protein eluted in a single well-defined peak at the elution volume consistent with a monomeric assembly in solution (Fig. S2) and it was concentrated up to 9 mg/mL. Therefore, with an optimized expression and purification protocol, we managed to obtain the pure monodisperse protein in a yield that was consistent with crystallization trials. The stability of the recombinant protein has been evaluated over time (1 week) at different temperatures (namely 20, 4 and −80 °C). By means of SDS/PAGE analysis and differential scanning fluorimetry (Fig. S3), we demonstrated that the protein does not undergo limited proteolysis or degradation upon time and that the melting temperature of the protein (57.6 °C) remains constant when measured on protein samples stored at different temperatures. Stability insights are further supported by protein activity not being altered over time.

Structural analysis of *Mt*DHODH

The best crystal of full-length *Mt*DHODH diffracted at 3.8 Å of resolution, and the structure shows the typical α/β TIM barrel fold common to other DHODHs, with the FMN molecule occupying an opening of the β-barrel core that is surrounded by eight α-helices (H4-H11; Fig. 2A). Unfortunately, the resolution range did not allow to detect the electron density of the substrate ORO. Residues 116–118 of chain A and residues 283–286 and 340–345 of chain B are absent from the model due to the local weak or missing electron density. Instead, a clear and unambiguous electron density map defines the N terminus, which allowed the reliable building of the so-far uncharacterized N terminus of *Mt*DHODH (Fig. S4). This region, stretching from amino acids 1–40 (3–40 in the structure model), caps the FMN cofactor and forms the binding site of the DHODHs inhibitors competitive with respect to the electron carrier molecules ubiquinone and MQ for *h*DHODH and *Mt*DHODH, respectively, as observed in their crystal structures (PDB codes 2PRM and 8OFW; Fig. 2B). In particular, the prosthetic group is positioned in its binding pocket mainly composed by loops that include residues Ala66, Asn241, Thr242, Ser263, Gly264, Gly292, Gly293, Gly313, Tyr314, and Thr315 establishing polar contacts with FMN (Fig. 2A). On the top of the β-barrel, beside the FMN there is the active site composed by the consensus sequence of class 2 DHODHs (Ser-Ser-Pro-Asn-Thr), housing the catalytic Ser179 that is oriented toward the FMN on the opposite side with respect to the N-terminal.

Comparative analysis with the human ortholog revealed a high degree of structural conservation between the two proteins (RMSD of C-alpha atomic positions between *Mt*DHODH and *h*DHODH is 0.93 Å). The main discrepancies reside at the N-terminal domain where the *h*DHODH misses the H3 helix (Ala32 to Leu41), which in the human protein is replaced by a long loop oriented toward the central core of the enzyme narrowing the ubiquinone-binding pocket and contributing to the steric hindrance as a possible element to be considered for selective molecules (see Discussion below). Moreover, *h*DHODH is characterized by an amino acidic insertion at level of H5 (aa 168–175 as numbered in human protein, PDB: 2PRM; Fig. 2B).

Biochemical characterization of *Mt*DHODH

*Mt*DHODH enzyme catalyzes the conversion of DHO into ORO using FMN as the oxidizing substrate that is further regenerated by the presence of another electron acceptor that, for the mycobacterial enzyme, corresponds to the MQ. Accordingly, the enzyme activity has been measured by means of DCIP as an alternative electron acceptor, as already demonstrated for other DHODHs [29–31]. The K_m value of
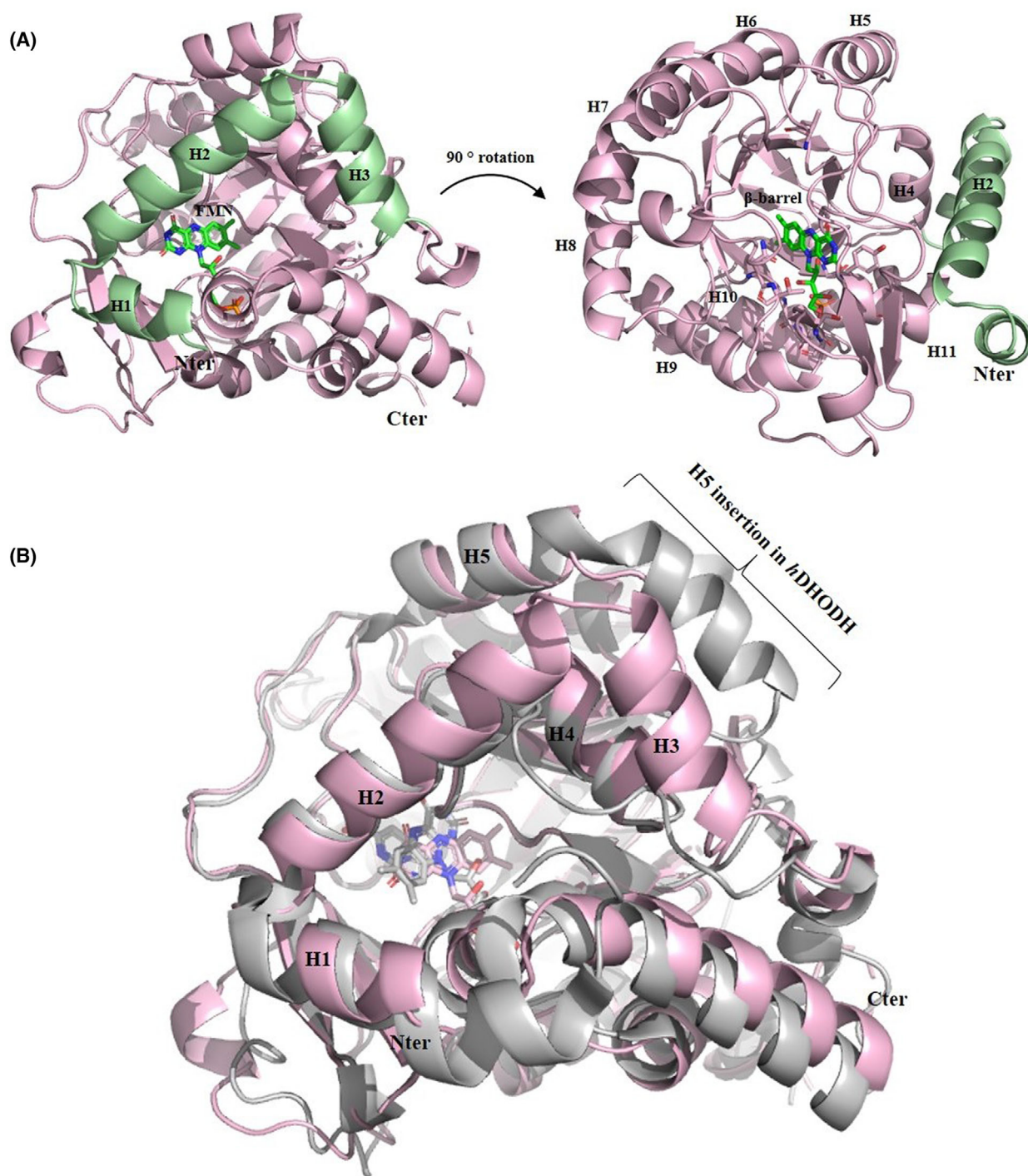
Fig. 2. (A) Cartoon representation of the *Mt*DHODH crystal structure, the N-terminal domain of the protein is depicted in pale green (left); on the right the view of the protein from the β-barrel with residues interacting with FMN showed as sticks. (B) Cartoon representation of *Mt*DHODH monomer (pink), optimally superimposed to the human DHODH (PDB: 2PRM); the two structures are centered on the three helices of the N-terminal domain of *Mt*DHODH housing the menaquinone-binding pocket.

recombinant, full-length *Mt*DHODH for the physiologic substrate was determined with DHO in presence of MQ obtaining an apparent K_m for DHO of 21.1 μM

and a k_{cat} of 17.84 min^{-1}. When MQ was used as substrate, maintaining fixed the concentration of DHO the enzyme exhibited a K_m for MQ of 54 μM and a
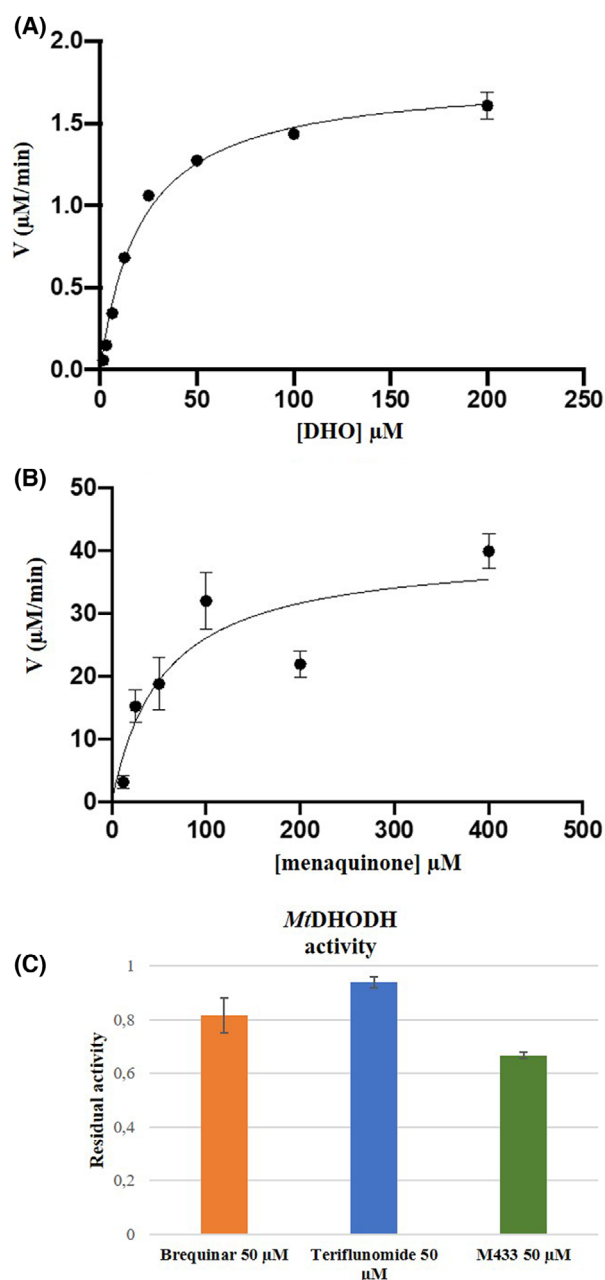
Fig. 3. Michaelis–Menten kinetics of the reaction catalyzed by *Mt*DHODH in the presence of DHO substrate (A) (1.6, 3.1, 6.2, 12.5, 25, 50, 100, and 200 μM), and menaquinone (B) (MQ) (12.5, 25, 50, 100, 200, and 400 μM). (C) *Mt*DHODH activity in the presence of 50 μM of human DHODH inhibitors.

k_{cat} of 401 min^{-1} (Fig. 3A,B), demonstrating that the DHO represents the rate-limiting factor of the reaction. Moreover, the protein activity was assayed over the range pH 6–10, using a series of constant ionic strength buffers. Fig. S5 shows the dependence of reaction velocity from pH profile, monitored by the DCIP assay. The enzyme shows an activity maximum at pH

9.0 and has no activity below pH 6.0. With the same experimental setting, we evaluated the capability of mycobacterial enzyme to use ubiquinone as oxidizing cofactor in order to validate the possibility of host-pathogen molecular cross talk at level of electron acceptor. The protein did not show enzymatic activity in presence of ubiquinone sustaining a potential selectivity of inhibitor molecules designed to interfere with *Mt*DHODH activity at level of quinone-binding site. To further test this hypothesis, well-characterized *h*DHODH inhibitors (namely Brequinar, Teriflunomide, and MEDS433) [15,32] were tested onto *Mt*DHODH and showed a maximum of 35% inhibitory activity when inhibitors were analyzed at 50 μM as concentration (Fig. 3C).

As depicted in Fig. 4A, an accurate structural analysis of quinone-binding sites can provide the molecular details for the development of selective *Mt*DHODH inhibitor. When compared, the host and the pathogen proteins revealed to have some similarities: the hydrophobic feature of the 'lipophilic patch' is predominantly maintained in accordance with the chemical properties of both ubiquinone and MQ molecules, whereas notable changes concern the peculiar substitution from *h*DHODH to *Mt*DHODH of Gln47 with Phe10, of Met43 with Arg6, of Pro365 with Glu322 and of Thr63 with Leu25, respectively. Among these discrepancies, the Gln47-to-Phe10 substitution could explain the lack of activity of some inhibitors that have been developed for the human ortholog (Fig. 3C). In particular, MEDS433 establishes an ion bridge extending to the side chain of Arg136 and a hydrogen bond with the side chain of Gln47 that is potentially lost in *Mt*DHODH [32]. Moreover, the molecular architecture of the N-terminal region of *Mt*DHODH is built on a three helices assembly, where the position of helix H3 strongly differs from the corresponding loop in *h*DHODH that is oriented toward the central core of the protein, narrowing the quinone-binding pocket (Fig. 4B). In order to achieve inhibitor selectivity, the modification of the chemical–physical environment at the level of the active site can be exploited to drive selective drug design.

Furthermore, Arg136 of *h*DHODH, paramount residue for inhibitors binding activities [15,32], is maintained in its identity in the MTB orthologue (Arg106), representing the key for an initial exploration of *h*DHODH inhibitor libraries.

Identification of a selective *Mt*DHODH inhibitor

In order to identify a selective *Mt*DHODH inhibitor to be considered as potential antimycobacterial agent,
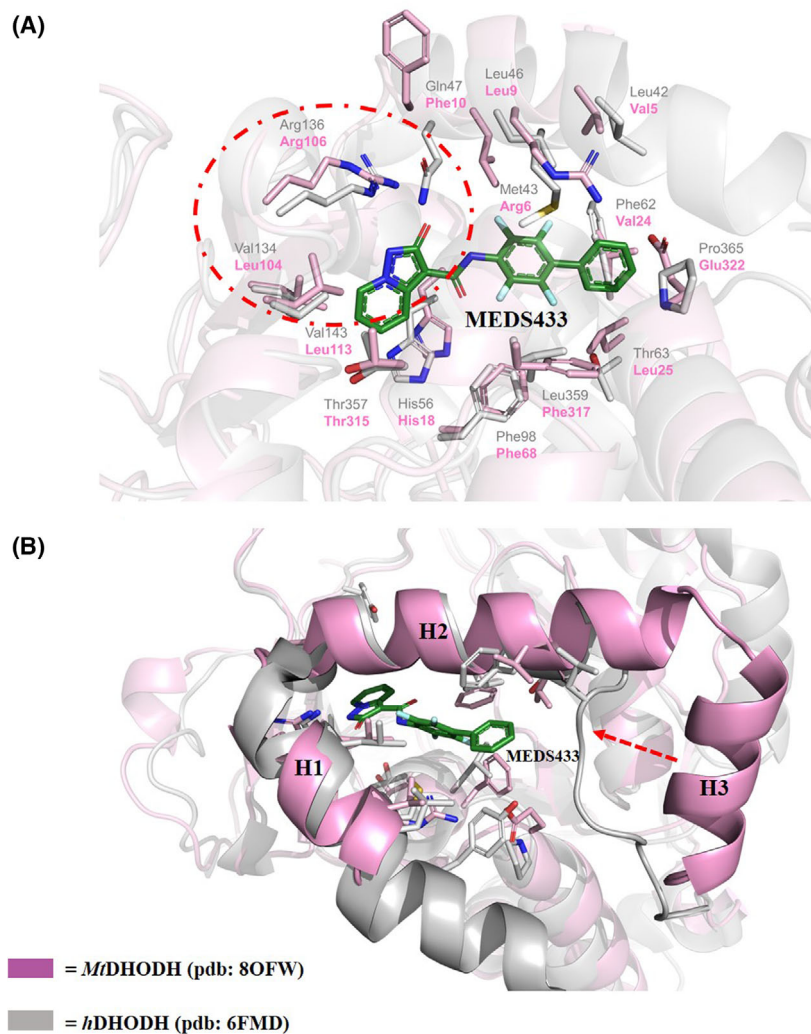
Fig. 4. (A) Cartoon representation of the optimally superimposed structures of *Mt*DHODH (chain B, this work) and hDHODH (PDB code 6FMD) in complex with MEDS433 inhibitor, at level of the quinone-binding site; MEDS433 (green) and relevant residues (gray) are rendered as sticks in the picture. (B) Close-up view of the active site of the quinone-binding site highlighting the steric hindrance of hDHODH as result of the position of the loop corresponding to H3 in *Mt*DHODH.

we screened our *in-house* chemical library consisting in more than 1200 compounds based on the hydroxyazoles scaffold and other heterocycles, with the characteristic of being carboxylic acid bioisosteres and able of establishing strong interactions with the positive ionized residues of proteins as arginine. Among them, we also included molecules, derived from the research pipelines aimed at identifying *human* [32–35] and *Plasmodium falciparum* DHODH inhibitors [36], that did not show activity toward their targets. The selection of potential *Mt*DHODH inhibitors from the *in-house* library has been performed following two basic principles: (i) identification of molecules having a chemical scaffold similar to others that have been reported with antimycobacterial activity; and (ii) presence of the carboxylic acid terminal or bioisosteres, potentially able of establishing strong interactions with the arginine located in the MQ binding pocket that is highly

conserved and interacts with most of the well-known DHODH inhibitors. With his approach, we identified 52 molecules that underwent *in vitro* investigation through enzymatic assay. Among them, compound **1** (hereafter MEDS322) resulted as the most potent molecule of the tested series. It contains the mentioned carboxylic acid and the thiazolidinone ring that is bioisostere of urea derivatives whose antimycobacterial activity was described by Brown and coauthors [37]. MEDS322, whose synthesis is described below and in the Scheme 1, inhibits *Mt*DHODH with an $IC_{50} = 43~\mu M$ (Fig. 5A) and represents the first selective inhibitor of *Mt*DHODH, since it showed no inhibitory activity on the human orthologue (produced as already described in reference [35]) (Fig. S1).

Furthermore, MEDS322 showed fluorescence emission at 530 nm following excitation at 350 nm (Fig. 5B), and additional proof of MEDS322 binding was
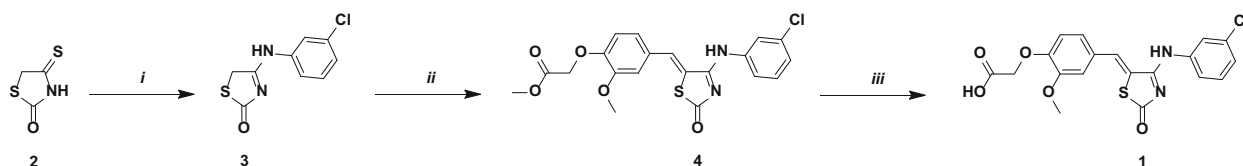
Scheme 1. Synthesis of compound **1**. (i) dry MeOH, 3-chloroaniline, reflux; (ii) methyl 2-(4-formyl-2-methoxyphenoxy)acetate, glacial acetic acid; (iii) 2 M NaOH, MeOH, r.t.
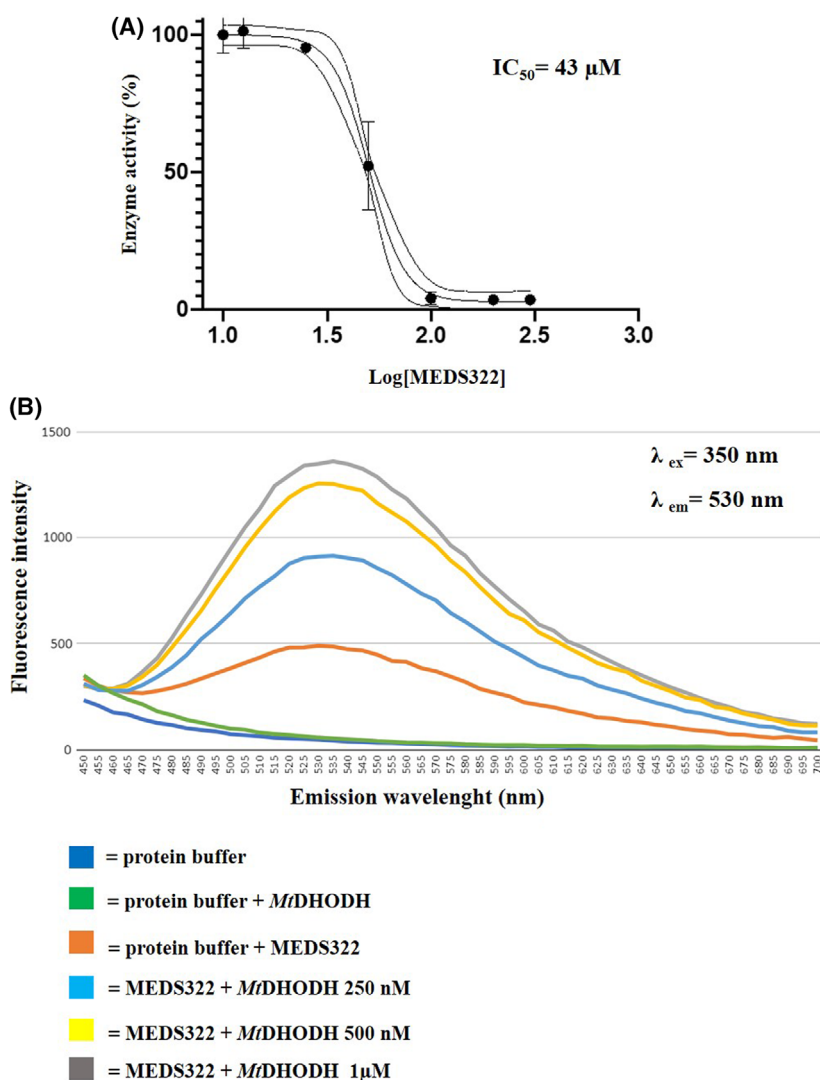
Fig. 5. (A) Graphical representation of MEDS322 IC50 for *Mt*DHODH; (B) Fluorescence emission spectra upon excitation at 350 nm of a solution containing 50 μM MEDS322, in the absence and presence of increasing concentration of *Mt*DHODH (namely 250 nM, 500 nM, 1 μM).

obtained by measuring the emission intensity of the molecule at increasing concentrations of *Mt*DHODH which resulted in an evident increase of the emission intensity, proportional to the protein concentration. As already demonstrated for other proteins having fluorometric properties [38,39], this effect could be attributed to the transition of MEDS322 from the polar environment of the bulk solvent to the quinone pocket that is characterized by a higher hydrophobicity.

The published structures of *h*DHODH in complex with various inhibitors together with the here reported first crystal structure of the full-length *Mt*DHODH allowed us to rationalize the molecular determinants of MEDS322 selectivity toward *Mt*DHODH.

Fig. 6. (A) Structure alignment of *Mt*DHODH (pink) with *h*DHODH (gray; PDB: 6FMD). Visualized is the N terminus of the proteins representing the menaquinone (MQ)/ubiquinone and inhibitors binding site of *Mt*DHODH and *h*DHODH, respectively. The three α-helices that shape the N terminus of *Mt*DHODH are named H1, H2, and H3 and are missing from the truncated structure of MtDHODH deposited in the PDB. The docked inhibitor MEDS322 and the superposed MEDS433 are shown in cyan and green, respectively; the interacting amino acids of MtDHODH are shown in pink sticks. The structured loop of hDHODH is shown in orange, highlighting its potential clashing with MEDS322 and rationalizing its selectivity toward MtDHODH. (B) Diagram of the molecular interactions of MEDS322 with residues of MtDHODH. Elements and molecules are color-coded and shown in sticks. Hydrogen bonds are labeled and shown as green dashed lines, and hydrophobic interactions are shown as red arcs.
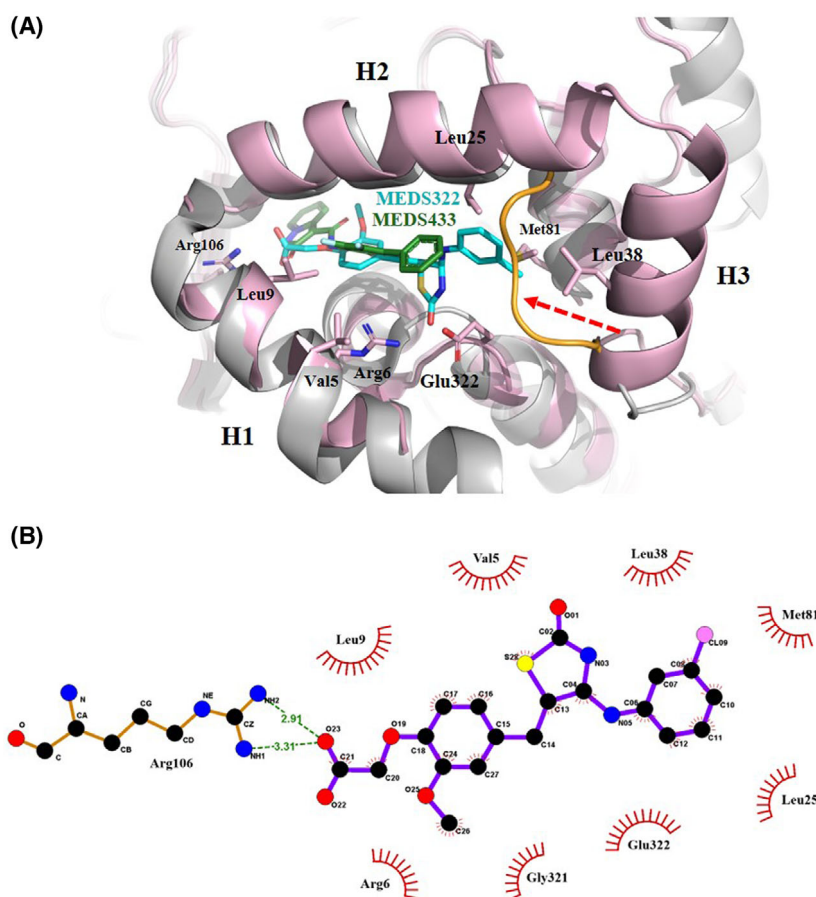
A representative binding pose of a *h*DHODH inhibitor and the related molecular interactions are reported by Sainas *et al.* [32], which showed the compound MEDS433 snugly inserted in the N-terminal ubiquinone-binding site which is constituted by helices H1 and H2 and a structured loop surrounding the inhibitor (amino acids Leu65-Ala71). Such binding pose guided the docking simulations of compound MEDS322 into the *Mt*DHODH experimental structure. This was performed using the HADDOCK server by imposing docking parameters consistent with the molecular interactions of compound MEDS433 to *h*DHODH [32]. However, in *Mt*DHODH, the structured loop of *h*DHODH is replaced by α-helix H3 (amino acids Ala32-Leu41) which enlarges the binding site and that we anticipated to drive inhibitor selectivity. Indeed, our docking simulations showed that the α-helix H3 of *Mt*DHODH is conveniently placed to accommodate the *Mt*DHODH-selective inhibitor MEDS322, whereas the structured loop of *h*DHODH clashes with the chloroaniline moiety of MEDS322, thus hampering its binding to *h*DHODH and rationalizing

its inefficacy on *h*DHODH inhibition and its selectivity for *Mt*DHODH.

Fig. 6 reports the docking of MEDS322 to *Mt*DHODH and the structural alignment with *h*DHODH in complex with MEDS433 inhibitor. *Mt*DHODH accommodates the MEDS322 ligand through the interaction of its carboxyl group with Arg106, thus anchoring and orienting the whole inhibitor. The docked molecule engages also in key hydrophobic interaction with residues Leu25 and with Leu38 of the structure, hence playing a determinant role in inhibition and selectivity (Fig. 6B). MEDS322, by targeting the quinone-binding site, sets the stage for a rational structure-based potency improvement for the identification of a lead compound to be further evaluated in *in vivo* tests. The molecule suffers the absence of an additional polar interaction with respect to the one established with Arg106; indeed, MEDS433 interacts also with Gln47 that is absent in *Mt*DHODH. A possible approach to increase the potency of future MEDS322 derivatives could be the functionalization of thiazolidinone ring to establish a polar interaction with Glu322 that in *h*DHODH is substituted by a proline residue (Fig. 6A).

Table 2. PreliminaryADME profiling for MEDS322.

	MEDS322
Thermodynamic solubility (μM)[a]	14.0 ± 0.6
Chemical stability[b]	>24 h
Plasma stability[c]	over 1 h
Plasma protein binding[d]	0.99
Metabolic stability[e]	83 ± 2%
logD$^{7.4}$ ± SE[f]	0.5 ± 0.1

[a]PBS pH 7.4, 24 h, room temperature. This analysis was performed by TechMed[III]. For details see supplementary material; [b]1 μM, RT, PBS pH 7.4, 5% DMSO, 24 h, room temperature. This analysis was performed by TechMed[III]. For details see supplementary material; [c]1 μM, 37 °C, CD-1 mouse plasma, 1 h. This analysis was performed by TechMed[III]. For details see supplementary material; [d]1 μM, 37 °C, CD-1 mouse plasma, 4 h. Fraction bound to proteins. This analysis was performed by TechMed[III]. For details see supplementary material; [e]1 μM, 37 °C, 0.5 mg/mL, human liver microsomes, cofactor: NADPH. % remaining compound after 1 h. This analysis was performed by TechMed[III]. For details see supplementary material; [f]Partition coefficients between *n*-octanol and PBS at pH 7.4 (log D$^{7.4}$) obtained using the shake-flask technique described in reference [41].

Synthesis of the MEDS322 compound

For the synthesis of target compound **1** a chemical strategy, which had already been investigated to obtain similar derivatives, was used [40]. The scheme starts from 1, 4-thioxo-2-thiazolidinone (isorhodanine) **2** that was allowed to react with 3-chloroaniline in refluxing methanol in order to obtain compound **3** in good yield and purity, with products precipitating from the reaction mixture and then collected by filtration. This latter was then condensed with methyl 2-(4-formyl-2-methoxyphenoxy)acetate involving a *Knoevenagel* condensation, performed in acetic acid as solvent, obtaining the target compound **4** as Z isomer. Compound **4** was hydrolyzed with 2 M NaOH to obtain the corresponding acid **1**.

MEDS322 preliminary ADME profiling

In order to complete the scenario, as the final step in this work, a preliminary ADME profile of MEDS322 was evaluated (Table 2 and Data S1). The compound presents an acceptable profile in terms of plasma stability and protein binding but its solubility falls in the lower limit to be considered acceptable. While this solubility profile did not preclude the *in vitro* studies on the compound, this property will be the first descriptor to improve during the following *hit-to-lead* process in order to reach acceptable drug-like properties for *in vivo* experiments.

Acknowledgements

Peer Review

The peer review history for this article is available at https://www.webofscience.com/api/gateway/wos/peer-review/10.1002/1873-3468.14680.

Data Accessibility

The structural data that support these findings are openly available in the wwPDB at https://doi.org/10.2210/pdb8OFW/pdb

References

1 WHO Global Tuberculosis Report 2022. Vol. **2022**, World Health Organization, Geneva.

2 WHO (2021) Meeting Report of the WHO Expert Consultation on the Definition of Extensively Drug-Resistant Tuberculosis, 27–29 October 2020. World Health Organization, Geneva.

3 Cole ST, Brosch R, Parkhill J, Garnier T, Churcher C, Harris D, Gordon SV, Eiglmeier K, Gas S, Barry CE III *et al.* (1998) Deciphering the biology of *Mycobacterium tuberculosis* from the complete genome sequence [published correction appears in nature 1998 Nov 12;396(6707):190]. *Nature* **393**, 537–544. doi: 10.1038/31159

4 Lipowska J, Miks CD, Kwon K, Shuvalova L, Zheng H, Lewiński K, Cooper DR, Shabalin IG and Minor W (2019) Pyrimidine biosynthesis in pathogens – structures and analysis of dihydroorotases from *Yersinia pestis* and *Vibrio cholerae*. *Int J Biol Macromol* **136**, 1176–1187. doi: 10.1016/j.ijbiomac.2019.05.149

5 Miggiano R, Morrone C, Rossi F and Rizzi M (2020) Targeting genome integrity in *Mycobacterium tuberculosis*: from nucleotide synthesis to DNA replication and repair. *Molecules* **25**, 1205.

6 Leung KY and Finlay BB (1991) Intracellular replication is essential for the virulence of salmonella typhimurium. *Proc Natl Acad Sci USA* **88**, 11470–11474. doi: 10.1073/pnas.88.24.11470

7 Fox BA and Bzik DJ (2002) *De novo* pyrimidine biosynthesis is required for virulence of toxoplasma gondii. *Nature* **415**, 926–929. doi: 10.1038/415926a

8 Samant S, Lee H, Ghassemi M, Chen J, Cook JL, Mankin AS and Neyfakh AA (2008) Nucleotide biosynthesis is critical for growth of bacteria in human blood. *PLoS Pathog* **4**, e37. doi: 10.1371/journal.ppat. 0040037

9 Warner DF, Evans JC and Mizrahi V (2014) Nucleotide metabolism and DNA replication. *Molecular Genetics of Mycobacteria* 633–656.

10 Sassetti CM, Boyd DH and Rubin EJ (2003) Genes required for mycobacterial growth defined by high density mutagenesis. *Mol Microbiol* **48**, 77–84. doi: 10. 1046/j.1365-2958.2003.03425.x

11 Reis RAG, Calil FA, Feliciano PR, Pinheiro MP and Nonato MC (2017) The dihydroorotate dehydrogenases: past and present. *Arch Biochem Biophys* **632**, 175–191. doi: 10.1016/j.abb.2017.06.019

12 Inaoka DK, Sakamoto K, Shimizu H, Shiba T, Kurisu G, Nara T, Aoki T, Kita K and Harada S (2008) Structures of *Trypanosoma cruzi* dihydroorotate dehydrogenase complexed with substrates and products: atomic resolution insights into mechanisms of dihydroorotate oxidation and fumarate reduction. *Biochemistry* **47**, 10881–10891. doi: 10.1021/bi800413r

13 Kubota T, Tani O, Yamaguchi T, Namatame I, Sakashita H, Furukawa K and Yamasaki K (2018) Crystal structures of FMN-bound and FMN-free forms of dihydroorotate dehydrogenase from *Trypanosoma brucei*. *FEBS Open Bio* **8**, 680–691. doi: 10.1002/2211-5463.12403

14 Rowland P, Nørager S, Jensen KF and Larsen S (2000) Structure of dihydroorotate dehydrogenase B: electron transfer between two flavin groups bridged by an iron-Sulphur cluster. *Structure* **8**, 1227–1238. doi: 10.1016/s0969-2126(00)00530-x

15 Liu S, Neidhardt EA, Grossman TH, Ocain T and Clardy J (2000) Structures of human dihydroorotate dehydrogenase in complex with antiproliferative agents. *Structure* **8**, 25–33. doi: 10.1016/s0969-2126(00)00077-0

16 Löffler M, Knecht W, Rawls J, Ullrich A and Dietz C (2002) Drosophila melanogaster dihydroorotate dehydrogenase: the N-terminus is important for biological function *in vivo* but not for catalytic properties *in vitro*. *Insect Biochem Mol Biol* **32**, 1159–1169. doi: 10.1016/s0965-1748(02)00052-8

17 Fagan RL and Palfey BA (2009) Roles in binding and chemistry for conserved active site residues in the class 2 dihydroorotate dehydrogenase from *Escherichia coli*. *Biochemistry* **48**, 7169–7178. doi: 10.1021/bi900370s

18 Dhiman RK, Mahapatra S, Slayden RA, Boyne ME, Lenaerts A, Hinshaw JC, Angala SK, Chatterjee D, Biswas K, Narayanasamy P *et al.* (2009) Menaquinone synthesis is critical for maintaining mycobacterial

viability during exponential growth and recovery from non-replicating persistence. *Mol Microbiol* **72**, 85–97. doi: 10.1111/j.1365-2958.2009.06625.x

19 Boschi D, Pippione AC, Sainas S and Lolli ML (2019) Dihydroorotate dehydrogenase inhibitors in anti-infective drug research. *Eur J Med Chem* **183**, 111681. doi: 10.1016/j.ejmech.2019.111681

20 Sulyok M, Rückle T, Roth A, Mürbeth RE, Chalon S, Kerr N, Samec SS, Gobeau N, Calle CL, Ibáñez J *et al.* (2017) DSM265 for plasmodium falciparum chemoprophylaxis: a randomised, double blinded, phase 1 trial with controlled human malaria infection [published correction appears in lancet infect dis. 2017 Jun;17(6):576]. *Lancet Infect Dis* **17**, 636–644. doi: 10. 1016/S1473-3099(17)30139-1

21 Minato Y, Gohl DM, Thiede JM, Chacón JM, Harcombe WR, Maruyama F and Baughn AD (2019) Genomewide assessment of *Mycobacterium tuberculosis* conditionally essential metabolic pathways. *mSystems* **4**, e00070–e00019. doi: 10.1128/mSystems.00070-19

22 Villela AD, Sanchez-Quitian ZA, Ducati RG, Santos DS and Basso LA (2011) Pyrimidine salvage pathway in *Mycobacterium tuberculosis*. *Curr Med Chem* **18**, 1286–1298. doi: 10.2174/092986711795029555

23 Flot D, Mairs T, Giraud T, Guijarro M, Lesourd M, Rey V, van Brussel D, Morawe C, Borel C, Hignette O *et al.* (2010) The ID23-2 structural biology microfocus beamline at the ESRF. *J Synchrotron Radiat* **17**, 107–118. doi: 10.1107/S0909049509041168

24 (1994) The CCP4 suite: programs for protein crystallography. *Acta Crystallogr D Biol Crystallogr* **50**, 760–763. doi: 10.1107/s0907444994003112

25 Adams PD, Afonine PV, Bunkóczi G, Chen VB, Davis IW, Echols N, Headd JJ, Hung LW, Kapral GJ, Grosse-Kunstleve RW *et al.* (2010) PHENIX: A comprehensive python-based system for macromolecular structure solution. *Acta Crystallogr D Biol Crystallogr* **66**, 213–221.

26 Emsley P and Cowtan K (2004) Coot: model-building tools for molecular graphics. *Acta Crystallogr D Biol Crystallogr* **60**, 2126–2132.

27 DeLano WL (2002) The PyMOL Molecular Graphics System. Delano Scientific, San Carlos. References – Scientific Research Publishing. https://www.scirp.org/(S(vtj3fa45qm1ean45vvffcz55))/reference/ReferencesPapers.aspx?ReferenceID=1958992

28 Björnberg O, Grüner AC, Roepstorff P and Jensen KF (1999) The activity of *Escherichia coli* dihydroorotate dehydrogenase is dependent on a conserved loop identified by sequence homology, mutagenesis, and limited proteolysis. *Biochemistry* **38**, 2899–2908.

29 Knecht W, Bergjohann U, Gonski S, Kirschbaum B and Löffler M (1996) Functional expression of a fragment of human dihydroorotate dehydrogenase by means of the baculovirus expression vector system, and

kinetic investigation of the purified recombinant enzyme. *Eur J Biochem* **240**, 292–301. doi: 10.1111/j.1432-1033.1996.0292h.x

30 Hines V, Keys LD 3rd and Johnston M (1986) Purification and properties of the bovine liver mitochondrial dihydroorotate dehydrogenase [published correction appears in J biol Chem 1987 Nov 5;262 (31):15322]. *J Biol Chem* **261**, 11386–11392.

31 Nonato MC, de Pádua RAP, David JS, Reis RAG, Tomaleri GP, D'Muniz Pereira H and Calil FA (2019) Structural basis for the design of selective inhibitors for *Schistosoma mansoni* dihydroorotate dehydrogenase. *Biochimie* **158**, 180–190. doi: 10.1016/j.biochi.2019.01.006

32 Sainas S, Pippione AC, Lupino E, Giorgis M, Circosta P, Gaidano V, Goyal P, Bonanni D, Rolando B, Cignetti A *et al.* (2018) Targeting myeloid differentiation using potent 2-Hydroxypyrazolo[1,5- a] pyridine scaffold-based human dihydroorotate dehydrogenase inhibitors [published correction appears in J med Chem. 2019 Feb 14;62(3):1696]. *J Med Chem* **61**, 6034–6055. doi: 10.1021/acs.jmedchem.8b00373

33 Sainas S, Pippione AC, Giorgis M, Lupino E, Goyal P, Ramondetti C, Buccinnà B, Piccinini M, Braga RC, Andrade CH *et al.* (2017) Design, synthesis, biological evaluation and X-ray structural studies of potent human dihydroorotate dehydrogenase inhibitors based on hydroxylated azole scaffolds. *Eur J Med Chem* **129**, 287–302. doi: 10.1016/j.ejmech.2017.02.017

34 Sainas S, Giorgis M, Circosta P, Gaidano V, Bonanni D, Pippione AC, Bagnati R, Passoni A, Qiu Y, Cojocaru CF *et al.* (2021) Targeting acute myelogenous leukemia using potent human dihydroorotate dehydrogenase inhibitors based on the 2-Hydroxypyrazolo[1,5-a]pyridine scaffold: SAR of the biphenyl moiety. *J Med Chem* **64**, 5404–5428. doi: 10.1021/acs.jmedchem.0c01549

35 Sainas S, Giorgis M, Circosta P, Poli G, Alberti M, Passoni A, Gaidano V, Pippione AC, Vitale N, Bonanni D *et al.* (2022) Targeting acute myelogenous leukemia using potent human dihydroorotate dehydrogenase inhibitors based on the 2-Hydroxypyrazolo[1,5-a]pyridine scaffold: SAR of the Aryloxyaryl moiety. *J Med Chem* **65**, 12701–12724. doi: 10.1021/acs.jmedchem.2c00496

36 Pippione AC, Sainas S, Goyal P, Fritzson I, Cassiano GC, Giraudo A, Giorgis M, Tavella TA, Bagnati R, Rolando B *et al.* (2019) Hydroxyazole scaffold-based plasmodium falciparum dihydroorotate dehydrogenase inhibitors: synthesis, biological evaluation and X-ray structural studies. *Eur J Med Chem* **163**, 266–280. doi: 10.1016/j.ejmech.2018.11.044

37 Brown JR, North EJ, Hurdle JG, Morisseau C, Scarborough JS, Sun D, Korduláková J, Scherman MS, Jones V, Grzegorzewicz A *et al.* (2011) The structure-activity relationship of urea derivatives as anti-tuberculosis agents. *Bioorg Med Chem* **19**, 5585–5595. doi: 10.1016/j.bmc.2011.07.034

38 Spyrakis F, Felici P, Bayden AS, Salsi E, Miggiano R, Kellogg GE, Cozzini P, Cook PF, Mozzarelli A and Campanini B (2013) Fine tuning of the active site modulates specificity in the interaction of O-acetylserine sulfhydrylase isozymes with serine acetyltransferase. *Biochim Biophys Acta* **1834**, 169–181. doi: 10.1016/j.bbapap.2012.09.009

39 Miggiano R, Valenti A, Rossi F, Rizzi M, Perugino G and Ciaramella M (2017) Every OGT is illuminated … by fluorescent and synchrotron lights. *Int J Mol Sci* **18**, 2613. doi: 10.3390/ijms18122613

40 Pinson JA, Schmidt-Kittler O, Frazzetto M, Zheng Z, Jennings IG, Kinzler KW, Vogelstein B, Chalmers DK and Thompson PE (2012) Synthesis and pharmacological evaluation of 4-Iminothiazolidinones for inhibition of PI3 kinase. *Aust J Chem* **65**, 1396–1404. doi: 10.1071/CH12140

41 Pippione AC, Kilic-Kurt Z, Kovachka S, Sainas S, Rolando B, Denasio E, Pors K, Adinolfi S, Zonari D, Bagnati R *et al.* (2022) New aldo-keto reductase 1C3 (AKR1C3) inhibitors based on the hydroxytriazole scaffold. *Eur J Med Chem* **237**, 114366. doi: 10.1016/j.ejmech.2022.114366

Supporting information

Additional supporting information may be found online in the Supporting Information section at the end of the article.

Data S1 Supporting Information.